

Feather-inspired Passive Flaps for Flow Control on a Finite Rectangular Wing

Ahmed K. Othman* and Aimy Wissa.†

Princeton University, Princeton, NJ, 08540

Bird wings are equipped with multiple flow control devices, one of which is the covert feathers. The covert feathers act as high-lift aeroelastic flow control devices for stall mitigation. This study investigates the performance characteristics of covert-inspired passive torsionally hinged flaps mounted on the suction side of a finite rectangular wing with AR = 4.67 at Re = 200,000. Wind tunnel experiments including force and flow field measurements are used to analyze the effect of flap location, hinge stiffness, and flap inertia on the wing aerodynamic forces (i.e., lift and drag) and the flow physics of the wing-flap system. Two post-stall α ranges are defined in the study: the partial stall regime ($19^{\circ} \le \alpha \le 26^{\circ}$) and the global stall regime ($28^{\circ} \le \alpha \le 36^{\circ}$). Results show that the flaps can reduce drag by up to 15% and improve lift by up to 5% in the partial stall regime. The leading edge flaps are effective in reducing drag in this regime since they can lessen the effect of induced drag at the wing tip, where the downwash effect is prominent, and decrease pressure drag at the wing areas with separated flow by bringing the shear layer closer to the wing surface, leading to a substantial overall drag reduction. In the global stall regime, the flaps reduce drag by up to 5% and improve lift by up to 20%. The leading edge flap mitigates flow separation in this regime by interacting with the shear layer. However, the lift increase for the flap cases leads to an induced drag penalty, counteracting the reduction in pressure drag, resulting in a minimal overall drag reduction. Furthermore, we show that the flap inertia and hinge stiffness control the flap deflection angle which in turn controls to the change in the lift and drag forces relative to the baseline case.

I. Nomenclature

 α = angle of attack, deg β = flap deflection angle, deg c = wing chord length, m b = wing semi-span, m S = wing surface area, m² C_L = coefficient of lift C_D = coefficient of drag

 $\Delta C_L\%$ = percentage change in lift relative to baseline wing $\Delta C_D\%$ = percentage change in drag relative to baseline wing

AR = wing aspect ratio

 f_y = integrated force on the wing in y-direction, N f_x = integrated force on the wing in x-direction, N

I = flap moment of inertia. kg.m² i_{β} = dimensionless flap moment of inertia K = hinge torsional stiffness, N.m.rad⁻¹ k_{β} = dimensionless hinge torsional stiffness

 X_{β} = chordwise flap location from the leading edge, m

 x_{β} = dimensionless chordwise flap location

 L_f = length of the flap, m = span of the flap. m

^{*}Graduate Research Assistant, Department of Mechanical and Aerospace Engineering, AIAA Student Member.

[†]Assistant Professor, Department of Mechanical and Aerospace Engineering, AIAA Member.

 ρ = fluid density, kg.m⁻³ Re = Reynolds number

 U_{∞} = freestream velocity, m.s⁻¹

II. Introduction and Background

Applications of small uncrewed aerial vehicles (SUAVs) are rapidly expanding; ranging from toys and package delivery to surveillance, mapping, and urban planning. To meet the demands of these various missions, SUAVs need to be able to perform complex maneuvers effectively, requiring an enhanced level of agility and maneuverability [1]. Birds operate at a similar Reynolds number range to SUAVs, $Re = O(10^5)$; however, they are far more superior and agile flyers due to the combination of their flight efficiency, the adaptability and anatomical structure of their wings, and the multiple flow control systems they are equipped with [2, 3]. One of these flow control systems is the coverts. The coverts are contour feathers that line the upper and lower surfaces of bird wings. The upper wing coverts, shown in Fig. 1a, have been observed to passively deploy in flight, especially during high angle of attack maneuvers and gusty conditions, suggesting that they operate as aeroelastic flow control devices for stall mitigation [4, 5]. Due to their simplicity, low power cost, and aerodynamic benefits, the coverts have inspired multiple engineering flow control adaptations that vary in terms of flexibility (e.g., rigid and flexible flaps) and mobility modes (e.g., static flaps, freely moving flaps, and torsionally hinged flaps) [6–11]. Most of the studies that looked at coverts-inspired flow control devices show that they can provide lift enhancement, especially at post-stall angles of attack. Meyer et al. conducted wind tunnel testing, numerical simulations, and flight testing and were able to show that freely moving flap on two different glider airfoils (HQ17 and HQ41) resulted in delaying separation and improving post-stall lift by more than 10% at $Re = 1 - 2 \times 10^6$ [8]. Bramesfeld and Maughmer performed a similar study at $Re = 1 \times 10^6$ on an S824 airfoil, and their results indicated that the flaps can increase the maximum lift by about 20% [12]. They attributed the lift enhancement to the pressure dam effect in which the flap blocks the reverse flow from propagating upstream, resulting in a lower pressure upstream of the flap. Moreover, Duan and Wissa examined the effect of rigid static coverts-inspired flaps located between 40% and 80% of the chord from the leading edge and found that these flaps can improve post-stall lift by up to 23% at Re = 200,000 [6]. Additionally, Nair and Goza [13] and Othman et al. [14] investigated how coverts-inspired passive torsionally hinged flaps can affect the flow physics and performance of two different 2D airfoils at two different flight regimes represented by two different Reynolds numbers, namely Re = 1,000 and Re = 200,000. Both studies show that passive torsionally hinged flaps can improve lift post-stall by more than 12%, and the structural parameters of the flaps (i.e., flap inertia and hinge stiffness) can be used to tune these lift enhancements [13, 14].

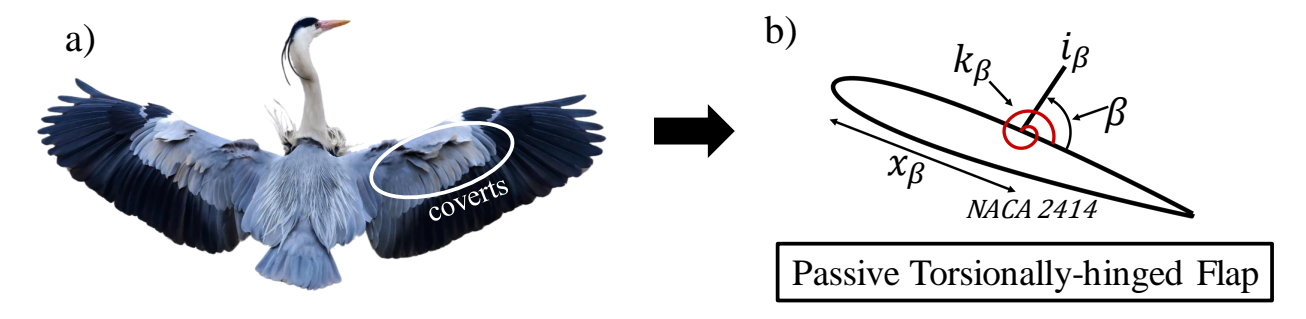


Fig. 1 a) Upper wing coverts on a heron wing [15]. b) Schematic of the torsionally-hinged passive flap system.

Most engineering studies on covert-inspired flaps have been on 2D airfoils [11, 13, 14, 16]. In this manuscript, we perform a detailed experimental analysis at a biologically relevant Reynolds number, Re = 200,000, to examine the effect of covert-inspired flaps located near the leading and trailing edge of a moderate AR finite rectangular wing on the aerodynamic forces (i.e., lift and drag) and the FSI physics for the wing-flap system. An AR of 4.67 was chosen due to its biological relevancy, especially for birds of prey that operate at this range of Re [17]. More specifically, we use a torsionally hinged flap analogy, shown in Fig. 1b, to represent the covert feathers. The deployment of the covert feathers is passive, meaning it mainly depends on the structural parameters of the feather, namely the rachis, which is the main feather shaft, and the two laterally attached vanes [18]. The coverts' deployment is mostly controlled by the shaft stiffness and the moment of inertia of the feather; therefore, a torsionally hinged flap where we can adjust the hinge stiffness and the flap inertia presents a biologically relevant analogy.

In this study, we utilize wind tunnel experiments, integrated force measurements, and particle image velocimetry (PIV) flow fields, to answer the following questions:

- Q1: How does a torsionally hinged flap affect the aerodynamic forces (i.e., lift and drag) post-stall at a Reynolds number $Re = O(10^5)$ for a rectangular wing?
- Q2: What are the flow physics associated with the resulting aerodynamic forces and how do they vary as a function of the flap's structural parameters (i.e., flap inertia and hinge stiffness)?

The remainder of the manuscript is organized as follows: Section III details the study parameters and experimental methods. Section IV presents the results for the integrated lift and drag forces along with the associated PIV flow fields and discusses the performance enhancement and FSI physics involved. Section V includes important conclusions and recommendations for future work.

III. Experimental Methodology

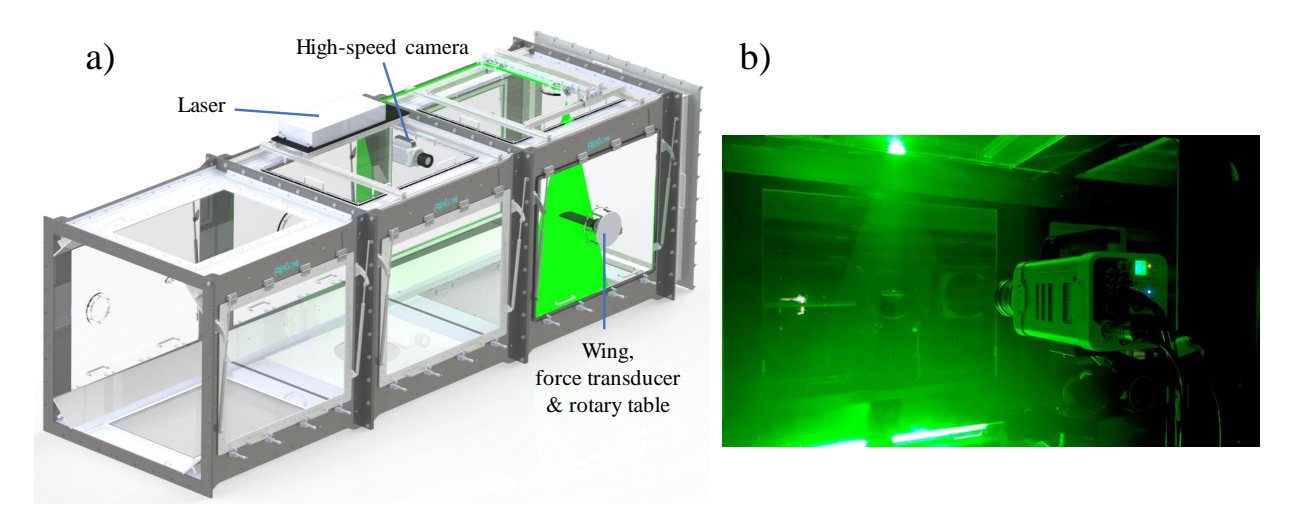


Fig. 2 a) A render of the experimental setup showing the wing, the wind tunnel, and the PIV system b) The wind tunnel, PIV, and camera setups.

A. Wing and flap design

In this study, we model the covert-feathers as passive torsionally hinged flaps located on the suction side of a semi-span finite rectangular wing. The wing cross-section is a NACA2414 airfoil (Fig. 1b) with a chord length c = 0.12m and a semi-span of b = 0.28m, resulting in an aspect ratio of AR = 4.67. This airfoil cross-section is chosen since it is well characterized in literature [11, 14, 19], and is suitable for SUAVs applications. The varying flap and hinge parameters in this study are the flap location, defined as the chord-wise distance of the flap from the leading edge, X_{β} , the flap moment of inertia, I, and the torsional stiffness of the hinge, K. These parameters are non-dimensionalized as,

$$i_{\beta} = \frac{I}{\rho L_f l_f^4}, \qquad k_{\beta} = \frac{K}{\rho U_{\infty}^2 L_f l_f^2}, \qquad x_{\beta} = \frac{X_{\beta}}{c}$$
 (1)

The reference length scales used here are the flap length l_f and span L_F , the reference velocity scale is the free stream velocity U_{∞} , and the reference density is the fluid density ρ_f . The parameters i_{β} , k_{β} and k_{β} are the non-dimensional counterparts of I, K and K_{β} . The flap location K_{β} is reported as percentage of the chord length from the leading edge in this manuscript. For example 0.2c flap refers to the flap hinged at 20% chord-length away from the leading edge. In this study, the length of the flap is fixed at 0.15c, and the span of the flap is set equal to the wing semi-span $L_f = b$, resulting in the flap covering the entire span of the tested wing. Moreover, two flap locations are tested, 0.2c and 0.7c, representing a leading edge (LE) and a trailing edge (TE) flap, respectively. The flap is mounted on the wing upper surface using 1 mm-thick Kapton tape along with several 3D printed flexible TPU 95A hinges. The torsional

flap hinge stiffness is varied by changing the number of the TPU 95A hinges from 0 to, 2, 4, and 8. All the resulting torsional stiffness at the hinge location in the study are in the range between 2×10^{-3} N.m/rad $\leq K \leq 32 \times 10^{-3}$ N.m/rad. Furthermore, two different materials with distinct densities are utilized to modify the flap's inertia and mass, namely Mylar and VeroWhite with an equivalent flap mass of 1 g and 10 g, respectively. This results in a moment of inertia of $I_{\beta} = 0.1 \times 10^{-6}$ Kg.m² for the Mylar flap and $I_{\beta} = 1 \times 10^{-6}$ Kg.m² for the VeroWhite flap. These flap parameters were specified based on several studies in the literature [6, 14, 20, 21]. Only a single flap is tested each run, and the flap deployment and movements are purely in response to the surrounding fluid and not due to any additional actuation or sensory inputs. All dimensionless varying flap parameters for the experiments are reported in Table 1.

Table 1 List of non-dimensional varying parameters for the experiments

	Dimensionless parameters	Values
Varying parameters	Flap location (x_{β})	{0.2, 0.7}
	Hinge stiffness (k_{β})	{0.02, 0.1, 0.2, 0.4}
	Flap moment of inertia (i_{β})	{3,30}

B. Wind tunnel testing facility

The wind tunnel experiments are performed in the closed-circuit low-speed wind tunnel at Princeton University. The exact specifications of this wind tunnel can be found in Breuer et al. [22]. Fig. 2a shows a render of the wind tunnel facility and the wing tested, and Fig. 2b shows an actual picture of the PIV and camera setups. The experiments are carried out in the third wind tunnel test section, which has a cross section of 1.2×1.2 m and a length of 1.4 m. The wind tunnel turbulence intensity is measured to be 0.03% of the free stream velocity. The experiments are carried out at chord-based Reynolds number Re = 200,000, corresponding to an equivalent free stream velocity of $U_{\infty} = 26$ m/s. During the experiments, the wing root is attached at the side door of the test section to a Velmex B48 rotary table with a stepper motor to vary the wing's angle of attack with a precision of 0.0125° . Meanwhile, the other end of the wing is left free to allow for tip vortices to form.

C. Force measurements

Force measurements are collected for angles of attack between 0° and 36° using a six-degree-of-freedom ATI Gamma force/torque transducer sampled at 1 kHz. lift L and drag D forces are calculated based on the measured aerodynamic loads in the wing's body frame f_x and f_y and the wing's angle of attack α

$$L = -f_v \cos(\alpha) - f_x \sin(\alpha), \quad D = -f_v \sin(\alpha) + f_x \cos(\alpha). \tag{2}$$

The coefficient of lift C_L and drag C_D are obtained by dividing the lift and drag forces by the dynamic pressure and the surface area of the wing S

$$C_L = \frac{L}{\frac{1}{2}\rho U_{\infty}^2 S}, \quad C_D = \frac{D}{\frac{1}{2}\rho U_{\infty}^2 S}.$$
 (3)

The force/torque transducer has a range of 0-32 N for both the x and y channels, a resolution of 1/160 N, and a maximum uncertainty equal to 0.75% of the full-scale load which is equivalent to a lift coefficient uncertainty $C_L = \pm 0.0175$ or $\pm 1.45\%$ of the full-scale range of measured lift coefficients in this study.

D. PIV flow field measurements

Time-resolved Planar particle image velocimetry (PIV) is used to obtain measurements of the flow around the wing, 3 cm inboard from the wing tip. The PIV setup includes a Photonics DMX high-speed Nd:YLF 527 nm dual cavity high-repetition laser with an acquisition rate of 1 kHz, which is mounted at the top of the wind tunnel test section as shown in Fig. 2a. The laser beam is redirected toward the area of interest via a series of 90° mirrors. Additionally, a series of adjustable converging and diverging lenses are used to adjust the width and focal length of the laser beam so that the focal point of the sheet lies in the center of the region of interest and the sheet's thickness is under 2 mm. The beam is then fanned out into a laser sheet using a -10 mm cylindrical lens. The laser sheet illuminates neutrally buoyant Di-Ethyl-Hexyl-Sebacat (DEHS) particles with an average diameter of 1 µm. Image pairs are then acquired using a

Photron Nova R5 high-speed CMOS camera with a full resolution of 9 MP. The acquired images are processed using multi-pass cross-correlation in LaVision's DaVis software. A 64×64 px interrogation window is used for the first three correlation passes, followed by a 24×24 px adaptive window for the following three passes, with 50% overlap between regions. The final PIV vector spacing is 0.82% of the chord length. 1000 frames obtained over the duration of 1 second are averaged to obtain the time-averaged flow fields presented in the results section.

IV. Results and Discussion

A. Overview of baseline wing characteristics

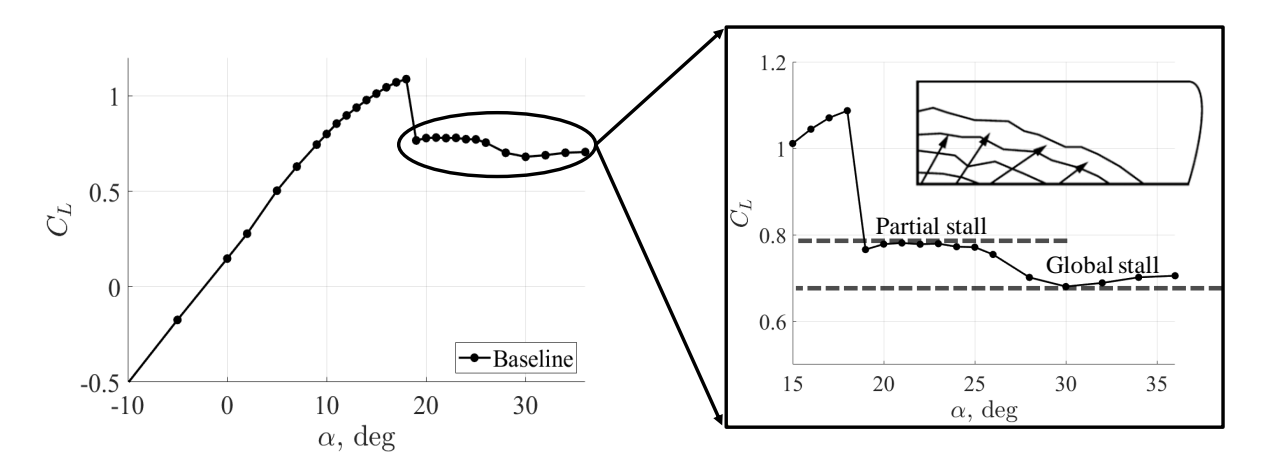


Fig. 3 Lift coefficient C_L versus α for the baseline wing. Zoomed-in region indicate the two post-stall regimes: partial stall and global stall. The schematic in the top right corner shows how stall propagates for a finite rectangular wing.

Fig. 3 shows the lift coefficient, C_L , as a function of the wing angle of attack, α for the baseline wing. The wing stalls at $\alpha = 19^{\circ}$ as demonstrated by the sudden drop in lift at this angle. Additionally, by taking a closer look at the post-stall angles of attack, we observe two C_L plateaus. The first plateau is between $\alpha = 19^{\circ} - 25^{\circ}$ which will be referred to as partial stall, and the second plateau is between $\alpha = 28^{\circ} - 36^{\circ}$, named global stall. The wing utilized in this study is rectangular; rectangular wings stall first at the trailing edge of the root, and as α increases, stall propagates till it reaches the leading edge of the tip, as shown in the schematic in Fig. 3 [23].

In the partial stall regime, the wing has a higher lift coefficient compared to global stall, indicating that there is still some attached flow as a result of the downwash from the tip vortices reducing the effective angle of attack at the wing tip. Thus, even though the overall wing lift coefficient has dropped, stall hasn't yet reached the wing tip since it is experiencing a relatively lower effective α ; hence the naming partial stall. As α increases furthermore, the C_L value drops into the second plateau, indicating that the whole wing is now experiencing global flow separation, hence the naming global stall.

Similar behavior can be observed from the $C_D-\alpha$ curve shown in Fig. 4, where C_D increases rapidly at $\alpha=19^\circ$. We see that at the partial stall regime, the $C_D-\alpha$ curve has a higher slope compared to the global stall regime, indicating extra lift-induced drag from the downwash at the wing tip adding to the pressure drag dominating the areas of the wing experiencing flow separation. As α increases further, the wing goes into global stall, and the $C_D-\alpha$ slope decreases. The reduction in the $C_D-\alpha$ slope in the global stall regime is due to the induced drag diminishing as C_L goes down into the second plateau, and pressure drag becoming the dominant factor here.

For the remainder of the study, We break our analysis into two stages. First, to answer the questions related to the effect of the flap on the aerodynamic forces post-stall for a rectangular wing (Q1), we will focus on the lift and drag force measurements and how they change as a function of the flap location, hinge stiffness, and flap inertia in both the partial and global stall regimes. We will then examine the PIV flow fields for the cases with the most significant aerodynamic benefits and where performance is most sensitive to the flap structural parameters to identify the flow physics and FSI mechanisms associated with those benefits (Q2).

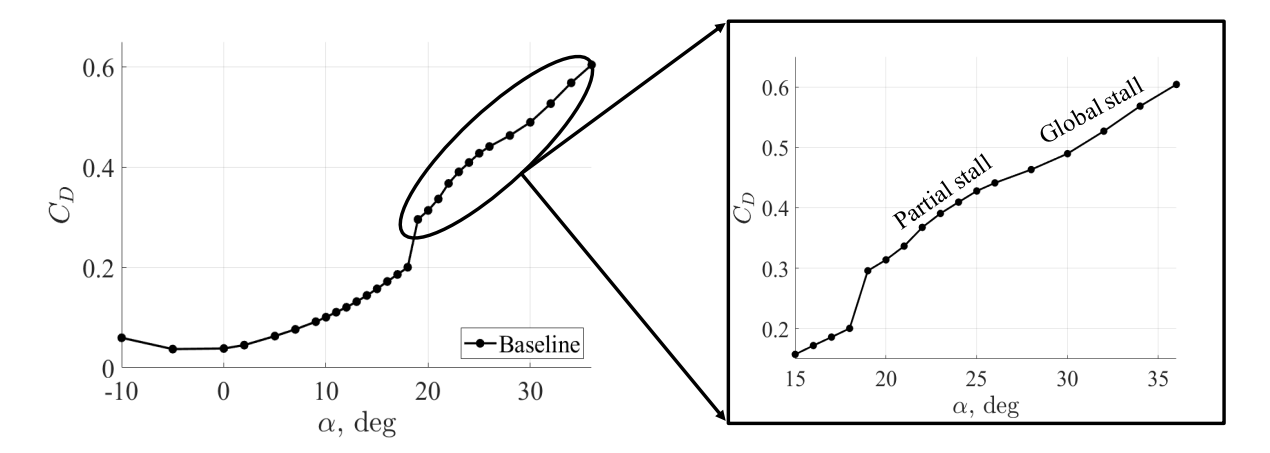


Fig. 4 Drag coefficient C_D versus α for the baseline wing. Zoomed-in region indicate the two post-stall: partial stall and global stall.

B. Effect of flap parameters on lift and drag

In this section, we examine the flap effects at post-stall conditions, where lift losses and drag increase are most limiting to SUAVs flight envelope, and where the covert feathers are also noticed to deploy in nature. We focus on one angle of attack in the partial stall regime, $\alpha = 24^{\circ}$ and one angle in the global stall regime, $\alpha = 32^{\circ}$. Fig. 5 shows the effect of the flap location, hinge stiffness, and flap inertia on the wing lift coefficient shown as a percentage change relative to the baseline flap-less case, $\Delta C_L \%$.

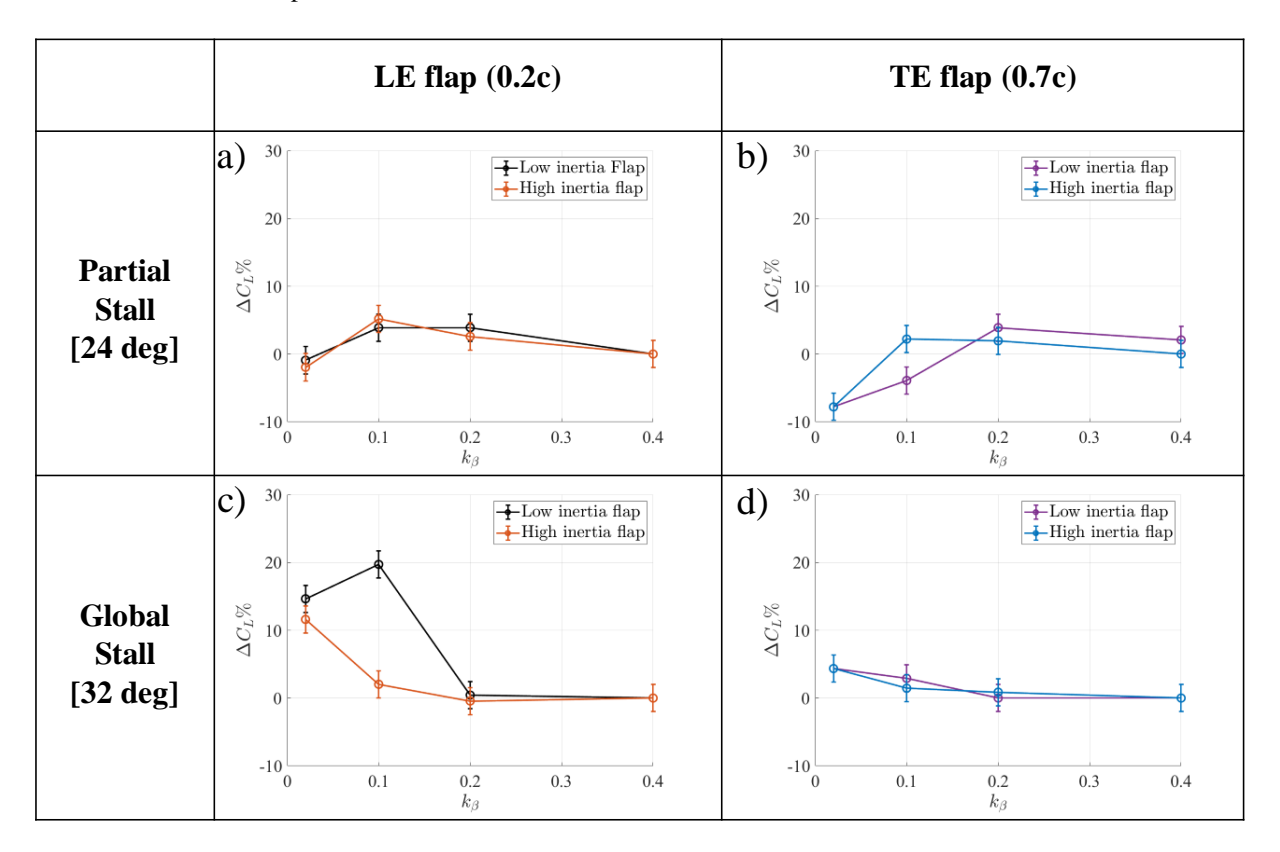


Fig. 5 Percent change in the lift coefficient ΔC_L % relative to the baseline wing as a function of the hinge stiffness k_β for the low and high inertia flaps at the leading edge flap location (a & c) and the trailing edge flap location (b & d) at partial stall $\alpha = 24^\circ$ (top row) and global stall $\alpha = 32^\circ$ (bottom row).

Fig. 5a indicates that the Leading edge (LE) flap has a minimal commensurate effect on the lift coefficient with $\Delta C_L \% \approx 0-5\%$ in the partial stall regime for both the low and high inertia flaps. However, in the global stall regime (Fig. 5c), the low inertia LE flap with the two lowest stiffnesses ($k_{\beta} = 0.02$ and $k_{\beta} = 0.1$) improve lift by 15% and 20%, respectively. However, as k_{β} increases beyond 0.1 (i.e. $k_{\beta} = 0.2$ and $k_{\beta} = 0.4$), ΔC_L % becomes 0, indicating that the flap no longer deploys due to the extra restoring torque imposed by the added stiffness. In contrast, only the lowest stiffness case for the high inertia LE flap improves lift by about 12%, whereas the rest of the cases result in no noticeable lift improvement in the global stall regime. The additional flap mass for the high inertia flap results in an additional restoring torque, limiting the hinge stiffness range for which the flap can deploy and improve lift. Furthermore, the trailing edge (TE) flap is detrimental to lift in the partial stall regime (Fig. 5b), where $\Delta C_L \% = -8\%$ for the lowest stiffness cases $k_{\beta} = 0.02$ for the low and high inertia flaps. As the stiffness k_{β} increases for the TE flap in the partial stall regime, the flap deflection angle decreases till the flap no longer deploys and ΔC_L % reaches 0. Conversely, in the global stall regime (Fig. 5d), the TE flap provides lift improvements with a maximum ΔC_L % = 5% for the lowest stiffness case, $k_B = 0.02$. As k_B increases, the lift improvement of the TE flap decreases, implying that as the deflection angle decreases, the TE flap lift improvement decreases till the flap no longer deploys and ΔC_L % reaches 0. Both the LE and TE flaps are more effective at improving lift in the global stall regime because the flow is fully separated over the entire wing, thus a flap covering the entire wing can mitigate this separation and provide significant lift benefits. Nevertheless, in the partial stall regime, where the flow is still attached near the tip for the baseline wing, the flap deployment result in global flow separation over the entire wing at the flap hinge location. The flap inducing flow separation at the tip region for the partial stall regime would result in making the flap either detrimental to lift as in the case of the TE flap (Fig. 5b) or diminish the overall lift benefits for the LE flap (Fig. 5a).

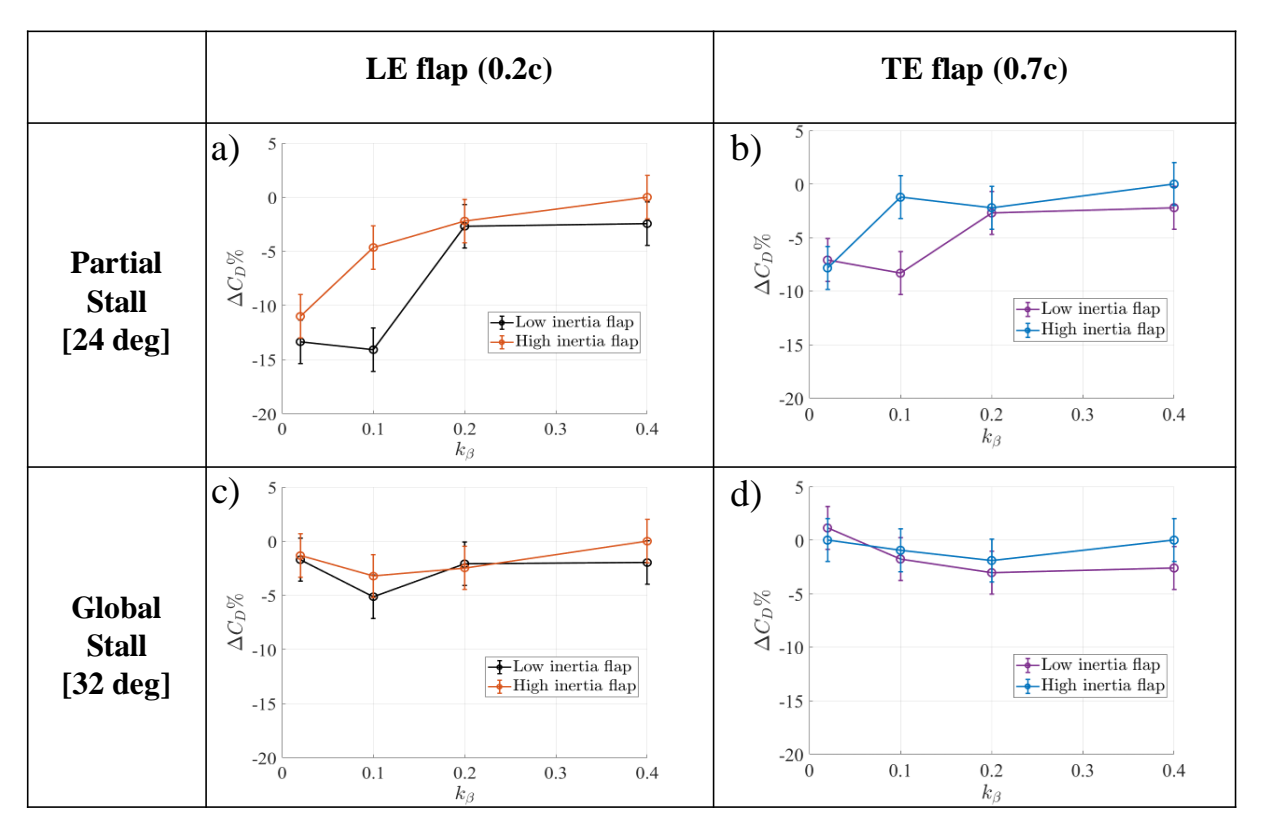


Fig. 6 Percent change in the drag coefficient ΔC_D % relative to the baseline wing as a function of the hinge stiffness k_β for the low and high inertia flaps at the leading edge flap location (a & c) and the trailing edge flap location (b & d) at partial stall $\alpha = 24^\circ$ (top row) and global stall $\alpha = 32^\circ$ (bottom row).

Fig. 6 shows the effect of the flap location, hinge stiffness, and flap inertia on the drag of the wing relative to the baseline flap-less case, ΔC_D %. The low inertia LE flap provides up to 15% reduction in drag, in the partial stall regime (Fig. 6a). For the high inertia flap, only the lowest k_β case provides significant drag reduction, $\Delta C_D = -11$ %. Additionally, the TE flap also reduces drag by up to 8% for the low inertia flap and 7% for the high inertia flap (Fig. 6b).

The trends are the same as the ones shown in Fig.5, where the two lowest k_{β} cases result in significant drag reduction for the low inertia flap at the two flap locations, while only the lowest stiffness case is effective for the high inertia flap due to the extra imposed restoring torque from the additional flap mass not allowing the flap to effectively deploy. The reason passive-torsionally hinged flaps are providing significant drag reduction while not showing a significant lift improvement at the partial stall regime is that the flaps reduce pressure drag by mitigating flow separation in the stalled region of the wing as shown in multiple studies before [6, 8, 11, 13]. Moreover, near the tip, where downwash and induced drag are still significant, and the flow is not fully separated for the baseline wing, the flap can mitigate induced drag by inducing flow separation in this region, thus decreasing the effect of downwash and tip vortices and reducing induced drag.

On the other hand, both the LE and TE flaps result in minimal drag reduction in the global stall regime (Fig.6 c and d) with a maximum of about 5% for the LE flap, and 3% for the TE flap. This is due to the flap improving lift in the global stall regime as shown in Fig.5 c and d, recovering some of the pressure differential between the upper and lower surfaces of the wing. This pressure differential and improved lift result in an induced drag penalty, since it enhances the formation of tip vortices and increases downwash. The extra induced drag penalty in the global stall regime diminishes the drag reduction resulting from mitigating flow separation and reducing pressure drag, leading to a minimal total ΔC_D %.

C. PIV flow fields of the LE flap configurations

In this section, we analyze the time-averaged flow field to understand the flow physics associated with the post-stall lift and drag benefits. We focus on the LE flap for two main reasons. First, it provides the highest lift improvements and drag reduction, as shown in Fig. 5 and Fig. 6. Additionally, changes in the LE flap structural parameters result in significant changes in the performance enhancements. Fig. 7 shows the time-averaged vorticity contours with superimposed streamlines for the leading edge flap cases that experienced significant flap deployment, resulting in lift improvement or drag reduction in both the partial and global stall regimes. Comparing the plots for the baseline cases in Fig. 7a and Fig. 7e, one observes that the wing experiences flow separation from the leading edge in the global stall regime at $\alpha = 32$, compared to partial stall where the flow remains attached up until roughly 20% chord length from the leading edge. One would expect that even more of the flow over the wing will be attached in the partial stall regime as we move further outboard toward the wing tip for this rectangular wing.

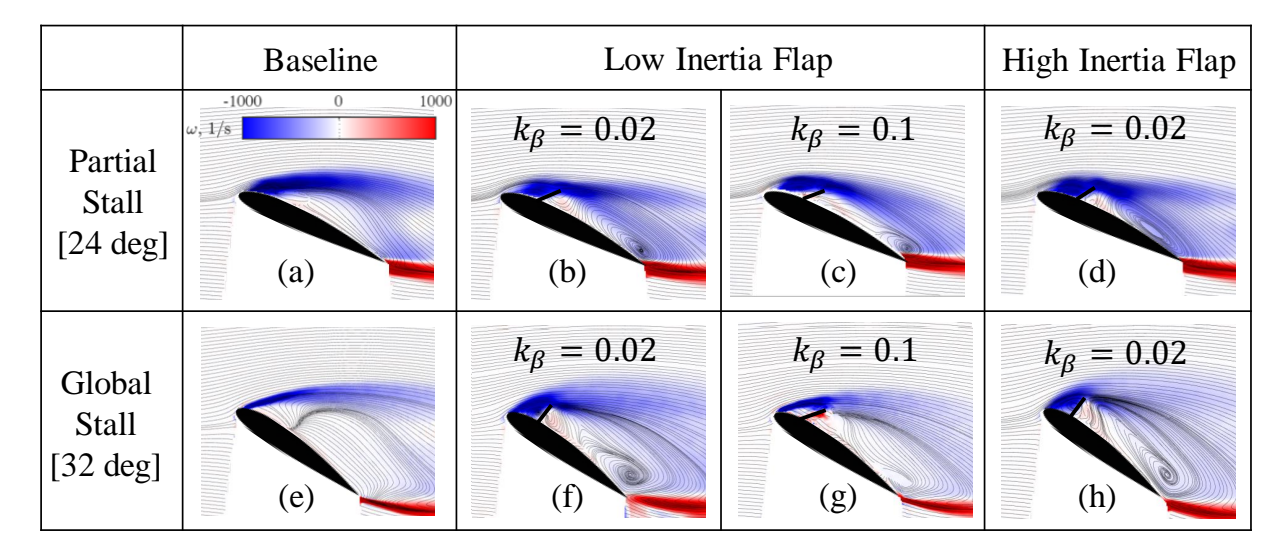


Fig. 7 Time-averaged PIV flow field showing the vorticity contours superimposed with the streamlines, where the top row (a, b, c, and d) show the baseline and LE flap cases at partial stall $\alpha = 24^{\circ}$ and the bottom row (e, f, g, and h) show the baseline and LE flap cases at global stall $\alpha = 32^{\circ}$.

1. Partial stall regime $[\alpha = 24^{\circ}]$

In Fig. 7, the first row of plots (Fig. 7a - d), shows the flow fields of the baseline and LE flap cases at the partial stall regime. Comparing the flow fields of the baseline to the flap cases, we notice that all the cases with a LE flap interact

with the shear layer, making it more diffused downstream of the flap. The diffused shear layer for the flap cases appears to have larger parts closer to the wing surface relative to the baseline. Moreover, a consistent recirculation region can be observed downstream of the flap, with its center located near the trailing edge of the wing, along with a smaller wake for the flap cases compared to the baseline case. The smaller wake and the aforementioned induced drag reduction, explain why these bio-inspired passive torsionally-hinged flaps result in the drag reduction at the partial stall regime as observed in Fig. 6a.

2. Global stall regime $[\alpha = 24^{\circ}]$

The second row of plots (Fig. 7e - h) shows the flow fields of the baseline and LE flap cases at the global stall regime. First, we notice some recirculating flow developing upstream of the flap for the low stiffness cases $k_{\beta} = 0.02$ in both the low and high inertia flaps due to their high deflection angles. Second, the deployment of the LE flap here reduces the geometric adverse pressure gradient the flow experiences along the wing's surface at this high angle of attack, bringing the shear layer closer to the surface and reducing the degree of flow separation, which explains the resulting lift improvements shown in Fig. 5c. Furthermore, as k_{β} increases from 0.02 to 0.1 for the low inertia flap (Fig. 7f and Fig. 7g), the mean flap deflection angle decreases, bringing the edge of the shear layer even closer to the wing surface, and the flow no longer circulates upstream of the flap resulting in this case having the maximum lift improvement as shown in Fig. 5c.

V. Conclusions and Future Work

This study explores the effectiveness of covert-inspired passive torsionally hinged flaps mounted on the suction side of a finite moderate aspect ratio rectangular wing at Re = 200,000. The study aims to answer two main questions related to the aerodynamic benefits of the flaps (Q1), and the main flow physics and FSI mechanisms associated with these benefits (Q2). The results for the first question (Q1) show that the flaps can reduce drag by up to 15% and improve lift by up to 5% in the partial stall regime ($19^{\circ} \le \alpha \le 26^{\circ}$). Meanwhile, In the global stall regime ($28^{\circ} \le \alpha \le 36^{\circ}$), the flaps reduce drag by up to 5% and improve lift by up to 20%. For the second question (Q2), the study reveals that coverts-inspired flaps improve drag in the partial stall regime by decreasing the wake size behind the wing resulting in a pressure drag reduction along with minimizing the effect of downwash and induced drag. Moreover, in the global stall regime, the flaps improve lift by mitigating flow separation through a shear layer interaction mechanism, where the flap deflects the shear layer closer to the wing surface. The results also demonstrate that the flap inertia and hinge stiffness control the flap deflection angle, which governs the resulting aerodynamic benefits. This study can inform the design of adaptive flow control devices that fit within the power and volume constraints of SUAVs, especially with their rapidly expanding range of applications and diverse missions. Future studies can explore the effectiveness of covert-inspired flaps on variable aspect ratio wings and examine multiple span-wise flow fields, especially near the tip and root of the wing, to have a better understanding of the flow features across the wing-span.

References

- [1] Fahlstrom, P. G., Gleason, T. J., and Sadraey, M. H., Introduction to UAV systems, John Wiley & Sons, 2022.
- [2] Evers, J. H., "Biological Inspiration for Agile Autonomous Air Vehicles," Tech. rep., Air Force Research Lab, Eglin AFB, Munitions Directorate, 2007.
- [3] Othman, A. K., Zekry, D. A., Saro-Cortes, V., Lee, K. J. P., and Wissa, A. A., "Aerial and aquatic biological and bioinspired flow control strategies," *Communications Engineering*, Vol. 2, No. 1, 2023, p. 30.
- [4] Carruthers, A. C., Thomas, A. L., and Taylor, G. K., "Automatic Aeroelastic Devices in the Wings of a Steppe Eagle Aquila Nipalensis." *The Journal of Experimental Biology*, Vol. 210, No. Pt 23, 2007, pp. 4136–4149. https://doi.org/10.1242/jeb.011197.
- [5] Brown, R., and Fedde, M., "Airflow Sensors in the Avian Wing," Journal of Experimental Biology, Vol. 179, 1993, pp. 13-30.
- [6] Duan, C., and Wissa, A., "Covert-inspired flaps for lift enhancement and stall mitigation." *Bioinspiration & biomimetics*, Vol. 16, No. 4, 2021.
- [7] Zekry, D. A., Nam, T., Gupta, R., Zhu, Y., and Wissa, A. A., "Covert-inspired flaps: an experimental study to understand the interactions between upperwing and underwing covert feathers," *Bioinspiration & Biomimetics*, Vol. 18, No. 4, 2023, p. 046021.

- [8] Meyer, R., Hage, W., Bechert, D. W., Schatz, M., Knacke, T., and Thiele, F., "Separation Control by Self-Activated Movable Flaps," *AIAA journal*, Vol. 45, No. 1, 2007, pp. 191–199.
- [9] Othman, A. K., Nair, N. J., Sandeep, A., Goza, A., and Wissa, A., "Numerical and Experimental Study of a Covert-Inspired Passively Deployable Flap for Aerodynamic Lift Enhancement," AIAA AVIATION 2022 Forum, 2022. https://doi.org/10.2514/6.2022-3980.
- [10] Bechert, D., Bruse, M., Hage, W., Meyer, R., Bechert, D., Bruse, M., Hage, W., and Meyer, R., "Biological surfaces and their technological application-laboratory and flight experiments on drag reduction and separation control," 28th Fluid dynamics conference, 1997, p. 1960.
- [11] Sedky, G., Simon, N., Othman, A. K., Wiswell, H., and Wissa, A., "Distributed feather-inspired flow control mitigates stall and expands flight envelope," *Proceedings of the National Academy of Sciences*, Vol. 121, No. 45, 2024, p. e2409268121. https://doi.org/10.1073/pnas.2409268121, URL https://www.pnas.org/doi/abs/10.1073/pnas.2409268121.
- [12] Bramesfeld, G., and Maughmer, M. D., "Experimental Investigation of Self-Actuating, Upper-Surface, High-Lift-Enhancing Effectors," *Journal of aircraft*, Vol. 39, No. 1, 2002, pp. 120–124.
- [13] Nair, N. J., and Goza, A., "Fluid-structure interaction of a bio-inspired passively deployable flap for lift enhancement," *Phys. Rev. Fluids*, Vol. 7, 2022, p. 064701. https://doi.org/10.1103/PhysRevFluids.7.064701, URL https://link.aps.org/doi/10.1103/PhysRevFluids.7.064701.
- [14] Othman, A. K., Nair, N. J., Goza, A., and Wissa, A., "Feather-inspired flow control device across flight regimes," *Bioinspiration & Biomimetics*, Vol. 18, No. 6, 2023, p. 066010.
- [15] Pixabay, 2020. URL https://pixabay.com/photos/animal-rural-grass-bird-wild-bird-4958086/.
- [16] Nair, N. J., Flynn, Z., and Goza, A., "Numerical Study of Multiple Bio-Inspired Torsionally Hinged Flaps for Passive Flow Control," Fluids, Vol. 7, No. 2, 2022. https://doi.org/10.3390/fluids7020044, URL https://www.mdpi.com/2311-5521/7/2/44.
- [17] Taylor, G. K., Carruthers, A. C., Hubel, T. Y., and Walker, S. M., Wing Morphing in Insects, Birds and Bats: Mechanism and Function, John Wiley Sons, Ltd, 2012, Chap. 2, pp. 11–40. https://doi.org/10.1002/9781119964032.ch2, URL https://onlinelibrary.wiley.com/doi/abs/10.1002/9781119964032.ch2.
- [18] Bachmann, T., Emmerlich, J., Baumgartner, W., Schneider, J. M., and Wagner, H., "Flexural stiffness of feather shafts: geometry rules over material properties," *Journal of Experimental Biology*, Vol. 215, No. 3, 2012, pp. 405–415. https://doi.org/10.1242/jeb.059451, URL https://doi.org/10.1242/jeb.059451.
- [19] Duan, C., and Wissa, A., "Covert-inspired flaps for lift enhancement and stall mitigation," Bioinspiration & Biomimetics, 2021.
- [20] Brücker, C., and Weidner, C., "Influence of self-adaptive hairy flaps on the stall delay of an airfoil in ramp-up motion," *Journal of Fluids and Structures*, Vol. 47, 2014, pp. 31–40.
- [21] Wang, L., Alam, M. M., and Zhou, Y., "Experimental study of a passive control of airfoil lift using bioinspired feather flap," *Bioinspiration & biomimetics*, Vol. 14, No. 6, 2019, p. 066005.
- [22] Breuer, K., Drela, M., Fan, X., and Di Luca, M., "Design and performance of an ultra-compact, low-speed, low turbulence level, wind tunnel for aerodynamic and animal flight experiments," *Experiments in Fluids*, Vol. 63, No. 11, 2022, p. 169.
- [23] Anderson, J. D., John D., Fundamentals of aerodynamics, 3rd ed., McGraw-Hill series in aeronautical and aerospace engineering, McGraw-Hill, Boston, 2001.